

Only if this paper was rejected by Computer Vision and Image Understanding, the author would like to submit it to other printing journals.

IEOPF: An Active Contour Model for Image Segmentation with Inhomogeneities Estimated by Orthogonal Primary Functions

Chaolu Feng^{a,b,*}

^a*Key Laboratory of Medical Image Computing of Ministry of Education, Northeastern University, Shenyang, Liaoning 110819, China*

^b*School of Computer Science and Engineering, Northeastern University, Shenyang, Liaoning 110014, China*

Abstract

Image segmentation is still an open problem especially when intensities of the interested objects are overlapped due to the presence of intensity inhomogeneity (also known as bias field). To segment images with intensity inhomogeneities, a bias correction embedded level set model is proposed where Inhomogeneities are Estimated by Orthogonal Primary Functions (IEOPF). In the proposed model, the smoothly varying bias is estimated by a linear combination of a given set of orthogonal primary functions. An inhomogeneous intensity clustering energy is then defined and membership functions of the clusters described by the level set function are introduced to define a data term energy of the proposed model. Similar to popular level set methods, a regularization term and an arc length term are also included to regularize and smooth the level set function, respectively. The proposed model are then extended to multichannel and multiphase pattern to segment colourful images and images with multiple objects. It has been extensively tested on both synthetic and real images that are widely used in the literature and public BrainWeb and IBSR datasets. Experimental results and comparison with state-of-the-art methods demonstrate that advantages of the proposed model in terms of bias correction and segmentation accuracy.

Keywords: image segmentation, bias correction, level set, orthogonal primary function

1. Introduction

Image segmentation is a fundamental but one of the most important problems in pattern recognition and computer vision [1]. In general, it aims at separating an image into several parts corresponding to meaningful objects. Inner elements (i.e., pixels for 2D images or voxels for 3D images) of each part, recognized as

*Corresponding author
Email address: fengchaolu@cse.neu.edu.cn (Chaolu Feng)

components of a desired object, are considered as having an identical characteristic in terms of shape, structure, or texture [2]. As well known, image segmentation has been extensively studied for decades and many efforts have been devoted to proposing effective methods, but it is still a challenging task to extract interested objects accurately from a complex image [3, 4]. In particular, if the image is corrupted by noise and bias field, intensity homogeneity of the image will be destroyed due to intensity overlaps between different objects, which certainly brings challenges to classical segmentation methods that are based upon edge detection or thresholding. Unfortunately, intensity inhomogeneities exist in most of real-world images inevitably. Fig. 1 gives an example to demonstrate negative effects of inhomogeneities on intensity distribution of a camera captured nature image and a medical brain image.

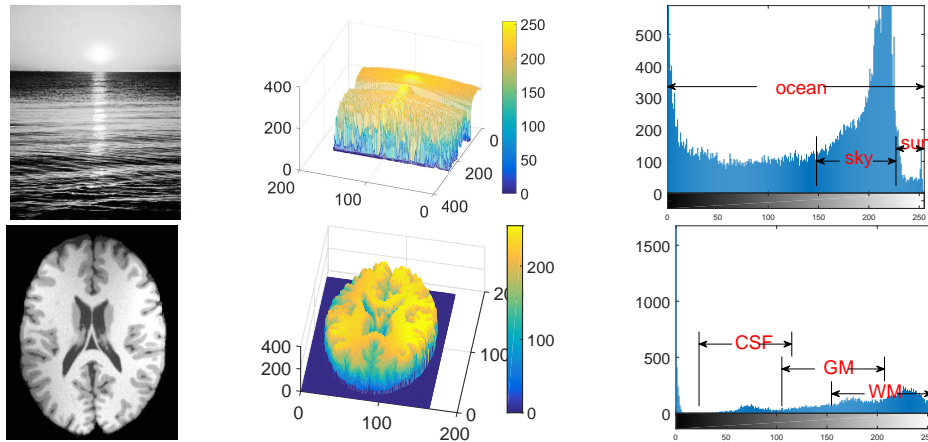


Figure 1: Intensity overlaps of interested objects in a camera image (upper) and an MR brain image (lower).

As mentioned earlier, a variety of segmentation methods have been proposed in the literature where active contour models (ACMs) have been extensively studied as one class of the most popular ones and have proven to be specially effective for image segmentation due to their ability to elastically deform and delineate object boundaries with smooth and closed contours in sub-pixel accuracy [5, 6]. The fundamental idea of ACMs is to introduce a contour to represent boundaries of interested objects and then drive the contour moving toward its interior normal direction under some constraints. The constraints are generally contained in a predefined energy function and the function will finally get its minimal value when the contour stops on true boundaries of the desired objects. However, there are inherent drawbacks of traditional ACMs, e.g., initialization sensitivity and difficulties associated with topological changes in merging and splitting of the evolving contour. Therefore, since the active contour model was proposed by Kass *et al.* in [7], many efforts have been devoted to developing improved methods to overcome the inherent drawbacks [8, 9]. As one of the most important improvements of ACMs, level set methods regard the active contour as the zero level set contour of a predefined one-dimension-higher function [10]. Motion of the contour is implied in evolution of the entire level set function under a principled energy minimization framework instead of directly

driving the contour itself. Therefore, interesting elastic behaviours of the active contour are preserved with topological changes of the contour efficiently handled by the evolution of the level set function. In addition, level set methods are easily extended to a higher dimension and prior knowledge of interested objects can be incorporated into their energy framework to guide the zero level set contour moves close to the desired boundaries [11, 12].

Existing level set methods are usually classified into edged-based and region-based methods depending on whether an edge indicator or a region descriptor is used to guide the motion of the zero level set contour. Edged-based level set methods are particularly efficient to recognize boundaries with sharp gradient, but they are not only generally sensitive to noise, but also often suffer from the boundary leakage problem especially in the vicinity of objects with weak boundaries [13]. The drawbacks are overcome in region-based level set methods by introducing region descriptors based on statistical information of the image in general to identify each region of interest [14]. In this paper, a region based level set model is proposed where bias correction is embedded in the model. Specifically, inhomogeneous intensities in the model are estimated by orthogonal primary functions. A demonstration of orthogonal Legendre functions in fitting smooth two dimensional functions is given in Fig. 2. We further extend the proposed model to segment multichannel images and images with multiple objects.

The rest of this paper is organized as follows. We first briefly review related work and some typical ACM models in Section 2. Details of the proposed model IEOPF are presented in Section 3. Experimental results of the proposed model on synthetic and natural images that are widely used in the literature and comparison with state-of-the-art models on BrainWeb and IBSR image repositories are given in Section 4. We analyse and discuss relationship and improvement of the proposed model with state-of-the-art model, its robustness to initialization, and coefficient impact in Section 5. This paper is finally summarized in Section 6.

2. Related Work

Let $\Omega \subset R^n$ be a n -dimensional continuous domain and I be an image defined on the domain. That is to say, the observed image can be viewed as a mapping from Ω to R . In general, the problem of image segmentation using ACMs is in fact to find a optimal contour C to separate the image I into two non-overlapping parts, i.e Ω_1 and Ω_2 , each of which is regarded as a desired object.

2.1. Classical Mumford-Shah functional model

To find the optimal contour C , Mumford and Shah proposed an energy based segmentation model via an energy functional in [15]. The basic idea of this classical model is to find a pair of (u, C) for a given image I , where u is a nearly piecewise smooth approximation of I . The general form of this functional can

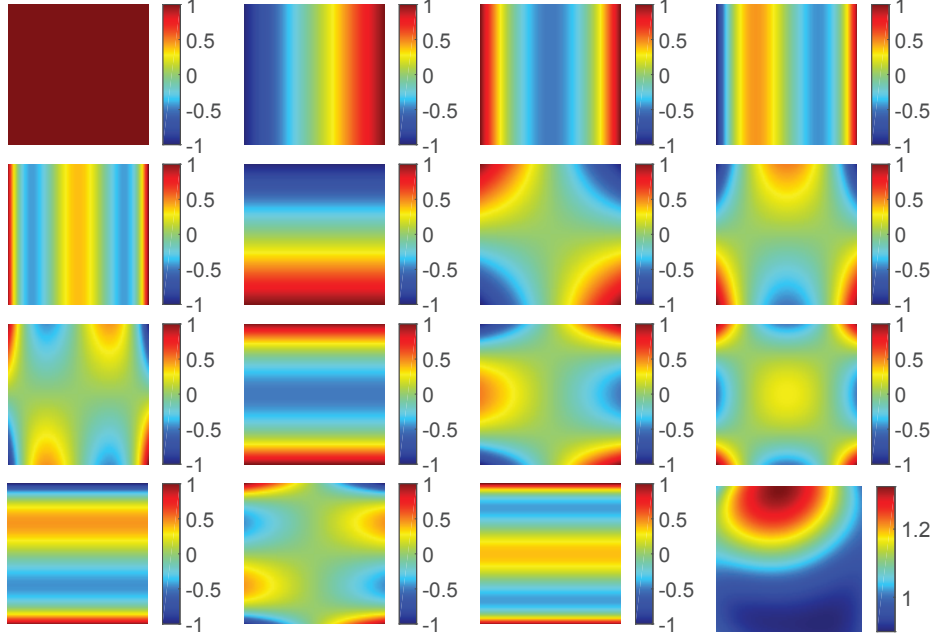


Figure 2: 15 2D orthogonal Legendre functions and the bias field (down-right) estimated using these functions with weighting coefficients 1.05, -0.05, -0.06, 0.01, 0.01, -0.20, 0.04, 0.12, -0.02, 0.02, 0.01, -0.02, 0.05, -0.03, -0.01 from up-left to down-right, respectively.

be written as

$$E_{MS}(u, C) = \int (u - I)^2 d\mathbf{x} + \mu \int_{\Omega \setminus C} |\nabla u| d\mathbf{x} + \nu |C| d\mathbf{x} \quad (1)$$

where μ and ν are positive weighting coefficients. Note that unless otherwise specified, integrations are all performed on the entire image domain Ω in this paper.

Remark 1. When the contour C is exactly located on the desired boundaries and u is piecewise smooth enough to approximate I , this functional takes its minimal value and vice versa. However, it is not easy to find the optimal solution of above defined energy functional due to different natures of the unknown C and u and the non-convexity of the functional as well.

2.2. Chan-Vese's piecewise constant model

To overcome the difficulties in solving Eq. (1), Chan and Vese proposed a piecewise constant case of the Mumford-Shah model in [16], which have proven to be particularly influential in binary segmentation. In the well known CV model, the contour C that separates the image I into two parts is considered as the 0-level set contour of a level set function ϕ , i.e. $C \triangleq \{\mathbf{x} : \phi(\mathbf{x}) = 0\}$. Function values of ϕ are opposite in sign on either side of the 0-level set contour. We let the level set function ϕ takes respectively negative and positive values in regions Ω_1 and Ω_2 which locate inside and outside the 0-level set contour C , i.e. $\Omega_1 \triangleq \{\mathbf{x} : \phi(\mathbf{x}) < 0\}$ and $\Omega_2 \triangleq \{\mathbf{x} : \phi(\mathbf{x}) > 0\}$. Thus, membership functions $M_1(\phi(\mathbf{x})) = 1 - H(\phi(\mathbf{x}))$ and

$M_2(\phi(\mathbf{x})) = H(\phi(\mathbf{x}))$ can be respectively used to represent these two regions by making $M_1(\phi()) = 1$ for $\mathbf{x} \in \Omega_1$, $M_2(\phi()) = 1$ for $\mathbf{x} \in \Omega_2$, and otherwise both of them are 0. Note that H is the Heaviside function. Then, the energy functional of the CV model is defined by

$$E_{CV}(c_1, c_2, \phi) = \sum_{i=1}^2 \int |I(\mathbf{x}) - c_i|^2 M_i(\phi(\mathbf{x})) d\mathbf{x} + \mu \mathcal{A}(\phi) + \nu \mathcal{L}(\phi) \quad (2)$$

where $\mathcal{A}(\phi) = \int (1 - H(\phi(\mathbf{x}))) d\mathbf{x}$ is the area enclosed by the 0-level set contour C , $\mathcal{L}(\phi) = \int |\nabla H(\phi(\mathbf{x}))| d\mathbf{x}$ is the length of the 0-level set contour C , μ and ν are positive weighting coefficients, and c_1 and c_2 are two constants that are used to approximate average intensities of the given image I on either side of the 0-level set contour C . It is obvious that c_1 and c_2 are related to the global properties of the image intensities in Ω_1 and Ω_2 , respectively. This model has also been further extended to segment images into multiple parts using multiphase level set functions [17]. But the CV model and its multiple phase extension are both on account of the assumption that intensities of the image are statistically homogeneous in each part and use different constants to estimate intensities of these parts. They are therefore well-known as piecewise constant (PC) models, which will fail to segment images with intensity inhomogeneity when disordered intensity distribution introduces overlaps between interested objects.

Remark 2. That is to say that even though the CV model is robust to some extent with respect to noise and is also less sensitive to the initialization, it generally fails to segment images with intensity inhomogeneity [16].

2.3. The piecewise smooth model

In addition to introduction of a local energy term as proposed in [18] or improving original global energy by means of introducing image local characteristics in [19], two similar ACMs were proposed by Vese and Chan [17] and Tsai *et al.* [20] instead under the frame work of minimization of the Mumford-Shah functional to overcome the difficulty of the CV model in segmentation of images with intensity inhomogeneity. These models are widely known as piecewise smooth (PS) models where the image intensities are considered as two piecewise smooth functions instead of constants to represent intensities on both sides of the contour C [17] by minimizing

$$E_{PS}(u_1, u_2, \phi) = \sum_{i=1}^N \int |I(\mathbf{x}) - u_i(\mathbf{x})|^2 M_i(\phi(\mathbf{x})) d\mathbf{x} + \mu \sum_{i=1}^N \int |\nabla u_i|^2 M_i(\phi(\mathbf{x})) d\mathbf{x} + \nu \mathcal{L}(\phi) \quad (3)$$

where μ and ν are positive weighting coefficients.

Remark 3. Although intensity inhomogeneity can be handled to some extent in the piecewise smooth model, it is obvious that the involved update of u_1 and u_2 at each iteration will certainly increase the

computational burden due to solving of two partial differential equations on the entire image domain Ω [19]. In addition, the level set function of the above model has to be periodically re-initialized to a signed distance function, which not only introduces problems like when and how it should be performed, but also affects numerical accuracy in an undesirable way [21].

2.4. Region-scalable fitting model

To resolve undesirable effects caused by re-initialization, Li *et al.* first introduced the following distance regularization term to intrinsically maintain the regularity of the level set function during its evolution in [13] and then applied it to the region-scalable fitting (RSF) model to preserve the stability of the level set function [22]:

$$\mathcal{P}(\phi) = \int \frac{1}{2} (|\nabla \phi(\mathbf{x})| - 1)^2 d\mathbf{x}. \quad (4)$$

In [22], local region information are incorporated into region-based level set methods relying on the assumption that intensities are locally homogeneous. Specifically, for a given point $\mathbf{y} \in \Omega$, two fitting functions $f_1(\mathbf{y})$ and $f_2(\mathbf{y})$ are used to approximate image intensities in Ω_1 and Ω_2 , respectively. Let $\int K(\mathbf{x} - \mathbf{y}) |I(\mathbf{x}) - f_i(\mathbf{y})|^2 d\mathbf{y}$ where K is a normalized even function with the property $K(\mathbf{u}) \geq K(\mathbf{v})$, if $|\mathbf{u}| < |\mathbf{v}|$, and $\lim_{|\mathbf{u}| \rightarrow \infty} K(\mathbf{u}) = 0$. And taking all the center points \mathbf{y} in the image domain Ω into consideration, the following energy functional is defined in the RSF model:

$$E_{RSF} = \int \sum_{i=1}^2 e_f^i(\mathbf{x}) M_i(\phi(\mathbf{x})) d\mathbf{x} + \nu \mathcal{L}(\phi) + \mu \mathcal{P}(\phi) \quad (5)$$

where ν and μ are positive weighting coefficients and $e_f^i(\mathbf{x}) = \int K(\mathbf{x} - \mathbf{y}) |I(\mathbf{x}) - f_i(\mathbf{y})|^2 d\mathbf{y}$.

Wang *et al.* further extended the RSF model to distinguish regions with similar intensity means but different variances by introducing Gaussian distributions to describe the local image intensities [21]. This improvement is in fact based on the assumption that intensities of the image obey normal distribution. Nevertheless, the image intensities are not necessarily described by a specific distribution, i.e. the intensities vary in any positions and directions and so do the intensity inhomogeneities. Therefore, histogram of the intensities and local statistics regarding the intensity and the magnitude of gradient are used to drive the evolution of the zero level set contour [23, 24].

Remark 4. Although above mentioned RSF model and its improvements have shown powerful capability for segmenting images with intensity inhomogeneity, they are sensitive to the size of local scalable-region which is controlled by the kernel function K and the location of the initial contour [25]. In fact, if the size of the local scalable-region is not large enough to ensure pixels inside are belongs to two interested objects or the zero level set contour is initialized far from the boundaries, the image will be miss-segmented or over-segmented. In addition, the above mentioned models have no capability to estimate the bias field and remove it from the inhomogenous image to be segmented.

2.5. Local intensity clustering model

To segment images with intensity inhomogeneity and simultaneously estimate the bias field, the local intensity clustering (LIC) model was proposed based on the assumptions that 1) the bias field b and the true image J are multiplicative components of a given image I and 2) the bias field is slowly and smoothly varying and the true image approximately takes distinct constant values c_1 and c_2 in disjoint regions Ω_1 and Ω_2 [26]. That is to say, in a small enough circular neighborhood of a given point $\mathbf{y} \in \Omega$, the bias field can be seen as a constant $b(\mathbf{y})$ and the standard K-means clustering can be used to classify intensities in the neighborhood. Taking all the center points of the entire image into account, the energy functional of the LIC model is defined by

$$E_{LIC} = \int \sum_{i=1}^2 e_b^i(\mathbf{x}) M_i(\phi(\mathbf{x})) d\mathbf{x} + \nu \mathcal{L}(\phi) + \mu \mathcal{P}(\phi) \quad (6)$$

where $e_b^i(\mathbf{x}) = \int K(\mathbf{x} - \mathbf{y}) |I(\mathbf{x}) - b(\mathbf{y})c_i|^2 d\mathbf{y}$, ν and μ are positive weighting coefficients, $M_1(\phi(\mathbf{x}))$ and $M_2(\phi(\mathbf{x}))$ are the membership functions of Ω_1 and Ω_2 , and K is a normalized function with properties described in section 2.4.

Remark 5. The LIC model has shown its powerful capability for segmenting the image and estimating the bias field simultaneously [26]. However, drawbacks associated with the RSF model in sensitivities to the size of local scalable-region and the location of initial contour still exist in the model [25]. In addition, there is no specific constraint on the bias field to ensure its slowly and smoothly varying property.

2.6. Local inhomogeneous intensity clustering model

To ensure its slowly and smoothly varying property, a given set of smooth orthogonal basis functions namely g_1, g_2, \dots , and g_M are introduced to fit the bias field in [27] in which the proposed model, i.e., Local Inhomogeneous iNtensity Clustering (LINC), is defined by

$$E_{LINC} = \int \sum_{i=1}^2 e_{\mathbf{w}}^i(\mathbf{x}) M_i(\phi(\mathbf{x})) d\mathbf{x} + \nu \mathcal{L}(\phi) + \mu \mathcal{P}(\phi) \quad (7)$$

where $e_{\mathbf{w}}^i(\mathbf{x}) = \int K(\mathbf{x} - \mathbf{y}) |I(\mathbf{x}) - \mathbf{w}^T G(\mathbf{y})c_i|^2 d\mathbf{y}$, $G(\mathbf{x})$ and \mathbf{w} are column vectors defined by $G(\mathbf{x}) = (g_1(\mathbf{x}), g_2(\mathbf{x}), \dots, g_M(\mathbf{x}))^T$ and $\mathbf{w} = (w_1, w_2, \dots, w_M)^T$, respectively, and w_1, w_2, \dots, w_M are weighting coefficients of the basis functions. Note that $(\cdot)^T$ is the transpose operator and all the other symbols represent the same meaning with those in section 2.5.

Remark 6. As demonstrated in [27], the LINC model has the capability in extracting desired objects accurately from noisy images and correcting the intensity biases simultaneously, and it is robust to initialization. Furthermore, the LINC model converges in less iterations than RSF and LIC [27]. However, convolution operation in the evolution results in a heavy computational burden.

3. Problem formulation

Given an intensity inhomogeneous image I defined on Ω , its intensities can be viewed as

$$I(\mathbf{x}) = b(\mathbf{x})J(\mathbf{x}) + n(\mathbf{x}) \quad (8)$$

where $I(\mathbf{x})$ and $J(\mathbf{x})$ are respectively the observed and true intensities at location \mathbf{x} of the image, b is the bias field accounting for the intensity inhomogeneity in the observed image, and n is additive zero-mean noise. In fact, the true image J can be assumed to be piecewise constant that characterizes an intrinsic physical property of objects being imaged, i.e., intensity c_i for the i -th type of objects. That is to say, the true image J approximately takes N distinct constant values c_1, c_2, \dots , and c_N in disjoint regions $\Omega_1, \Omega_2, \dots$, and Ω_N , respectively. The problem of image segmentation and bias correction is therefore considered as finding the specific intensity c_i for the i -th type of objects and estimating the bias field b at the same time.

3.1. Representation of the bias field

As well known, the bias field b is generally assumed to be slowly and smoothly varying in the literature. And a function can be theoretically approximated by a linear combination of a given number of primary functions up to arbitrary accuracy, only if the number of the basis functions is sufficiently large [28]. Therefore, we represent the bias field by a linear combination of a given set of smooth primary functions g_1, g_2, \dots , and g_M with weighting coefficients w_1, w_2, \dots , and w_m in this paper to ensure the smoothly varying property of b , i.e.,

$$b(\mathbf{x}) = \sum_{k=1}^M w_k g_k(\mathbf{x}) = \mathbf{w}^T G(\mathbf{x}) \quad (9)$$

where $(\cdot)^T$ is the transpose operator, $G(\mathbf{x})$ and \mathbf{w} are column vectors defined by $G(\mathbf{x}) = (g_1(\mathbf{x}), g_2(\mathbf{x}), \dots, g_M(\mathbf{x}))^T$ and $\mathbf{w} = (w_1, w_2, \dots, w_M)^T$, respectively. Note that the primary functions used in this paper are orthogonal and estimation of the bias field is performed by finding the optimal coefficients w_1, w_2, \dots, w_M .

3.2. Formulation for inhomogeneous intensity clustering

As mentioned earlier, the true image J approximately takes N distinct constant values in disjoint regions $\Omega_1, \Omega_2, \dots$, and Ω_N . Therefore, taking the constant intensity c_i of the true image J in Ω_i into account where $i = 1, 2, \dots, N$, intensities $b(\mathbf{x})J(\mathbf{x})$ in this region are close to $b(\mathbf{x})c_i$, i.e.,

$$b(\mathbf{x})J(\mathbf{x}) \approx b(\mathbf{x})c_i \quad \text{for} \quad \mathbf{x} \in \Omega_i. \quad (10)$$

Taking Eq. (9) into account, the above equation can be rewritten as

$$b(\mathbf{x})J(\mathbf{x}) \approx \mathbf{w}^T G(\mathbf{x})c_i \quad \text{for} \quad \mathbf{x} \in \Omega_i. \quad (11)$$

In consideration of the image model given in Eq. (8), we have

$$I(\mathbf{x}) \approx \mathbf{w}^T G(\mathbf{x}) c_i + n(\mathbf{x}) \quad \text{for} \quad \mathbf{x} \in \Omega_i. \quad (12)$$

As mentioned earlier, $n(\mathbf{x})$ is additive zero-mean noise. Therefore, we define the following inhomogeneous intensity clustering energy

$$\mathcal{F} = \sum_{i=1}^N \lambda_i \int_{\Omega_i} (I(\mathbf{x}) - \mathbf{w}^T G(\mathbf{x}) c_i)^2 d\mathbf{x} \quad (13)$$

where $\lambda_1, \lambda_2, \dots, \lambda_N$ are positive constants to indicate preference of the proposed model to the corresponding class. Note that when boundaries of the regions Ω_i for $i = 1, 2, \dots, N$ are exactly where they should be, the above defined energy takes its minimal value.

3.3. Two phase level set formulation IEOPF²

It is obvious that the proposed energy in Eq. (13) is expressed in terms of the regions $\Omega_1, \Omega_2, \dots$, and Ω_N , which makes it difficult to derive a solution to minimize the energy from this expression. In the case that the image domain Ω is separated into two disjoint regions Ω_1 and Ω_2 , i.e., $N = 2$, the energy defined in Eq. (13) can be converted to a level set formulation by representing the two disjoint regions with a given level set function ϕ defined on Ω . Then, the energy minimization problem can be solved by using well-established variational methods [26]. Let the level set function ϕ take negative and positive signs on either side of the 0-level set contour denoted by $C \triangleq \{\mathbf{x} : \phi(\mathbf{x}) = 0\}$, which can be used to represent a partition of the domain Ω with two disjoint regions. The disjoint regions separated by the contour can be represented by $\Omega_1 \triangleq \{\mathbf{x} : \phi(\mathbf{x}) < 0\}$ and $\Omega_2 \triangleq \{\mathbf{x} : \phi(\mathbf{x}) > 0\}$. In consideration of properties of the Heaviside function H , the regions are further represented by the following member functions $M_1(\phi(\mathbf{x})) = 1 - H(\phi(\mathbf{x}))$ and $M_2(\phi(\mathbf{x})) = H(\phi(\mathbf{x}))$, respectively. Thus, for the case $N = 2$, we rewrite the energy \mathcal{F} described in Eq. (13) into the following level set formulation

$$\mathcal{F} = \sum_{i=1}^2 \lambda_i \int (I(\mathbf{x}) - \mathbf{w}^T G(\mathbf{x}) c_i)^2 M_i(\phi(\mathbf{x})) d\mathbf{x} \quad (14)$$

It is obvious that the energy \mathcal{F} is a functional of variables the level set function ϕ , the vector $\mathbf{c} = (c_1, c_2)^T$, and the weight coefficients of the basis functions $\mathbf{w} = (w_1, w_2, \dots, w_M)^T$, i.e., $\mathcal{F}(\phi, \mathbf{c}, \mathbf{w})$. The energy $\mathcal{F}(\phi, \mathbf{c}, \mathbf{w})$ is the data term of the final energy functional of the proposed level set formulation, defined by

$$E(\phi, \mathbf{c}, \mathbf{w}) = \mathcal{F}(\phi, \mathbf{c}, \mathbf{w}) + \nu \mathcal{L}(\phi) + \mu \mathcal{P}(\phi) \quad (15)$$

where \mathcal{P} is the regularization term defined in Eq. (4) used here to maintain the regularity of the level set function ϕ and \mathcal{L} is the same arc length term used in state-of-the-art models to smooth the 0-level set contour.

Remark 7. The proposed model is essentially different from both LIC and LINC. First, there is no normalized even convolution kernel function in the proposed model and the integral is therefore one layer which is less than either LIC or LINC. Second, in the proposed method, an explicit constraint on the bias field is introduced to ensure the slowly and smoothly varying property of the bias field compared with LIC. Relationship of the proposed model with CV and PS will be discussed in Section 5.1.

3.4. Extension to multichannel case $IEOPF_L^2$

It is obvious that the above model defined in Eq. (15) is applicable in extracting interested objects from gray images. But multichannel images of the same scene that come from different imaging modalities or color images are becoming more and more common in our life. To extend the proposed model to be able to extract interested objects from multichannel images, we first denote a given multichannel image \mathbf{I} by $\mathbf{I} = (I_1, I_2, \dots, I_L)$ where L is the channel number of \mathbf{I} . Let $e_i(\mathbf{x}) = \sum_{j=1}^L \gamma_j (I_j(\mathbf{x}) - \mathbf{w}_j^T G(\mathbf{x}) \mathbf{c}_{ij})^2$ where γ_j are positive weighting coefficients that are used to control influence of the j -th channel. We then rewrite Eq. (14) as follows

$$\mathcal{F}(\phi, \mathbf{C}, \mathbf{W}) = \sum_{i=1}^2 \lambda_i \int e_i(\mathbf{x}) M_i(\phi(\mathbf{x})) d\mathbf{x} \quad (16)$$

where \mathbf{C} is an $2 \times L$ matrix defined by $\mathbf{C} = (\mathbf{c}_1, \mathbf{c}_2, \dots, \mathbf{c}_L)$ and \mathbf{W} is a matrix with $M \times L$ elements defined by $\mathbf{W} = (\mathbf{w}_1, \mathbf{w}_2, \dots, \mathbf{w}_L)$. We finally rewrite Eq. (15) as follows

$$E(\phi, \mathbf{C}, \mathbf{W}) = \mathcal{F}(\phi, \mathbf{C}, \mathbf{W}) + \nu \mathcal{L}(\phi) + \mu \mathcal{P}(\phi). \quad (17)$$

3.5. Further extension to multiphase case $IEOPF_L^N$

Since one level set function ϕ can only be used to represent 2 subregions of image domain Ω denoted by membership functions M_1 and M_2 , which are in fact inside and outside of the zero level contour of ϕ , Q level set functions are required to represent N subregions where $Q = \lceil \log_2(N) \rceil$. Thus, the subregion Ω_i can be represented by the member function $M_i(\Phi)$, i.e., $M_i(\Phi(\mathbf{x})) = 1$ for $\mathbf{x} \in \Omega_i$ and $M_i(\Phi_1(\mathbf{x})) = 0$ otherwise where $\Phi = (\phi_1, \phi_2, \dots, \phi_K)$ and $i = 1, 2, \dots, N$. To extend the proposed model to segment multiple objects from images with intensity inhomogeneity, we first further rewrite Eq. (16) as follows

$$\mathcal{F}(\Phi, \mathbf{C}, \mathbf{W}) = \sum_{i=1}^N \lambda_i \int e_i(\mathbf{x}) M_i(\Phi(\mathbf{x})) d\mathbf{x}. \quad (18)$$

We then define $\mathcal{P}(\Phi) = \sum_{q=1}^Q \mathcal{P}(\phi_q)$ and $\mathcal{L}(\Phi) = \sum_{q=1}^Q \mathcal{L}(\phi_q)$ where $\mathcal{P}(\phi_q) = (1/2) \int (|\nabla \phi_q(\mathbf{x})| - 1)^2 d\mathbf{x}$ and $\mathcal{L}(\phi_q) = \int |\nabla H(\phi_q(\mathbf{x}))| d\mathbf{x}$, respectively. Finally, we rewrite Eq. (17) as follows

$$E(\Phi, \mathbf{C}, \mathbf{W}) = \mathcal{F}(\Phi, \mathbf{C}, \mathbf{W}) + \nu \mathcal{L}(\Phi) + \mu \mathcal{P}(\Phi). \quad (19)$$

3.6. Energy minimization

In the proposed model, segmentation and bias correction are determined by the final level set function $\hat{\Phi}$ and the optimal weighting coefficients $\hat{\mathbf{W}}$ that are obtained by minimizing the energy functional $E(\Phi, \mathbf{c}, \mathbf{w})$ defined in Eq. (19). The energy minimization is achieved by an iterative process. That is to say, the energy functional $E(\Phi, \mathbf{C}, \mathbf{W})$ is minimized with respect to each of its variables Φ , \mathbf{C} , and \mathbf{W} in each iteration by fixing the other two with values from last iteration.

For fixed \mathbf{C} and \mathbf{W} , we minimize the energy functional $E(\Phi, \mathbf{C}, \mathbf{W})$ with respect to $\Phi = (\phi_1, \phi_2, \dots, \phi_Q)$ using the standard gradient descent method and obtain

$$\begin{aligned} \frac{\partial \phi_q}{\partial t} = & - \sum_{i=1}^N \frac{\partial M_i(\Phi)}{\partial \phi_q} \lambda_i e_i + \mu \left(\nabla^2 \phi_q - \operatorname{div} \left(\frac{\nabla \phi_q}{|\nabla \phi_q|} \right) \right) \\ & + \nu \delta(\phi_q) \operatorname{div} \left(\frac{\nabla \phi_q}{|\nabla \phi_q|} \right) \end{aligned} \quad (20)$$

where $q = 1, 2, \dots, K$.

For fixed Φ and \mathbf{W} , we minimize the energy functional $E(\Phi, \mathbf{C}, \mathbf{W})$ with respect to \mathbf{C} by solving the equation $\frac{\partial E}{\partial \mathbf{C}} = \mathbf{0}$ where $\mathbf{0}$ is a $N \times L$ matrix with constant value 0 and obtain

$$c_{ij} = \frac{\int (I_j(\mathbf{x}) \mathbf{w}_j^T G(\mathbf{x})) M_i(\Phi(\mathbf{x})) d\mathbf{x}}{\int (\mathbf{w}_j^T G(\mathbf{x}))^2 M_i(\Phi(\mathbf{x})) d\mathbf{x}} \quad (21)$$

where $i = 1, 2, \dots, N$ and $j = 1, 2, \dots, L$.

For fixed Φ and \mathbf{C} , we minimize the energy functional $E(\Phi, \mathbf{C}, \mathbf{W})$ with respect to \mathbf{W} by solving the equation $\frac{\partial E}{\partial \mathbf{W}} = \mathbf{0}$ where $\mathbf{0}$ is a $M \times L$ matrix with constant value 0 and obtain

$$\mathbf{w}_j = A_j^{-1} \mathbf{v}_j \quad (22)$$

where $j = 1, 2, \dots, L$ and A_j is a matrix with $M \times M$ elements and \mathbf{v} is an M -dimensional column vector, given by

$$A_j = \int \left(\sum_{i=1}^N \lambda_i c_{ij}^2 M_i(\phi(\mathbf{x})) \right) G(\mathbf{x}) G^T(\mathbf{x}) d\mathbf{x} \quad (23)$$

and

$$\mathbf{v}_j = \int \left(I_j(\mathbf{x}) \sum_{i=1}^N \lambda_i c_{ij} M_i(\phi(\mathbf{x})) \right) G(\mathbf{x}) d\mathbf{x}. \quad (24)$$

3.7. Implementation

In our numerical implementation, the Heaviside function H is approximated by a smooth version H_ϵ with $\epsilon = 1$, defined by

$$H_\epsilon(x) = \frac{1}{2} \left[1 + \frac{2}{\pi} \arctan \left(\frac{x}{\epsilon} \right) \right]. \quad (25)$$

The derivative of H_ϵ is used to approximate the Dirac delta function δ , which can be written as

$$\delta_\epsilon(x) = H'_\epsilon(x) = \frac{1}{\pi} \frac{\epsilon}{\epsilon^2 + x^2}. \quad (26)$$

In this paper, 15 orthogonal Legendre polynomial functions, which are four order precision, are used to approximately estimate the bias field, i.e., $M = 15$. In fact, for each $\mathbf{x} \in \Omega$, we can rewrite \mathbf{x} as $\mathbf{x} = (x_1, x_2)$ where x_1 and x_2 are directional components of the given two-dimensional image I defined on Ω . The smooth basis functions g_1, g_2, \dots , and g_{15} used in this paper are defined by $g_1(\mathbf{x}) = 1$, $g_2(\mathbf{x}) = x_1$, $g_3(\mathbf{x}) = (3x_1^2 - 1)/2$, $g_4(\mathbf{x}) = (5x_1^3 - 3x_1)/2$, $g_5(\mathbf{x}) = (35x_1^4 - 30x_1^2 + 3)/8$, $g_6 = x_2$, $g_7 = x_1x_2$, $g_8(\mathbf{x}) = (3x_1^2 - 1)x_2/2$, $g_9(\mathbf{x}) = (5x_1^3 - 3x_1)x_2/2$, $g_{10}(\mathbf{x}) = (3x_2^2 - 1)/2$, $g_{11}(\mathbf{x}) = x_1(3x_2^2 - 1)/2$, $g_{12}(\mathbf{x}) = (3x_1^2 - 1)(3x_2^2 - 1)/4$, $g_{13}(\mathbf{x}) = (5x_2^3 - 3x_2)/2$, $g_{14}(\mathbf{x}) = x_1(5x_2^3 - 3x_2)/2$, $g_{15}(\mathbf{x}) = (35x_2^4 - 30x_2^2 + 3)/8$. The column vector $G(\mathbf{x})$ can be therefore written as $G(\mathbf{x}) = (g_1(\mathbf{x}), g_2(\mathbf{x}), \dots, g_{15}(\mathbf{x}))^T$. The implementation of the proposed model can be straightforwardly expressed as follows in **Algorithm 1**.

Algorithm 1 The proposed bias correction embedded level set model IEOPF

Input: The multichannel image \mathbf{I} , its channel number L , and the number of interested objects N .

Output: Segmentation results determined by membership function $M_i(\Phi)$ and the bias field $\mathbf{b} = (b_1, b_2, \dots, b_L)$ with each b_j estimated by $\mathbf{w}_j^T G(\mathbf{x})$ where $i = 1, 2, \dots, N$ and $j = 1, 2, \dots, L$.

- 1: Initialize \mathbf{W} with a random $M \times L$ matrix and ϕ_k with a binary step function, defined by $\phi_q(\mathbf{x}) = -a$ for \mathbf{x} inside the initial zero-level contour of ϕ_q and $\phi_q(\mathbf{x}) = a$ otherwise, where $q = 1, 2, \dots, Q$.
 - 2: Update cluster center matrix \mathbf{C} with its elements c_{ij} computed using Eq.(21) where $i = 1, 2, \dots, N$ and $j = 1, 2, \dots, L$.
 - 3: Update ϕ_q by adding it with the difference determined by post-multiplying Eq.(20) with Δt where Δt represents the step of temporal difference and $q = 1, 2, \dots, Q$.
 - 4: Update the weighing coefficients matrix \mathbf{W} with each column of \mathbf{W} computed using Eq.(22).
 - 5: Check convergence criterion and iteration number. If convergence has been reached or the iteration number exceeds a predetermined maximum number, stop the iteration, otherwise, go to Step 2.
-

Note that the convergence criterion used in this paper is $\sum_{i=1}^N \sum_{j=1}^L \|c_{ij}^{(n+1)} - c_{ij}^{(n)}\|_2 < 0.001$, where $c_{ij}^{(n)}$ is the cluster center c_{ij} updated at the n -th iteration and $\|\star\|_2$ is the Euclidean distance of \star .

Remark 8. The main additional computational cost in the proposed model is for computing \mathbf{w}_j in Eq. (22) compared with state-of-the-art models reviewed in Section 2. However, we notice that $G(\mathbf{x})$ and $I_j(\mathbf{x})$ are independent of the level set functions Φ and clustering centers \mathbf{C} which indicate that we can compute $G(\mathbf{x})G^T(\mathbf{x})$ for Eq. (23) and $I_j(\mathbf{x})G(\mathbf{x})$ for Eq. (24) in advance and keep the results fixed during the iteration to accelerate the proposed model.

4. Experimental results

We have tested the proposed model extensively on synthetic and real images in Matlab R2016a on a computer with Intel(R) Core(TM)i5-3230M 2.6GHzCPU,4GBRAM,and Windows7 64-bit operating system.

In this section, we first evaluate effectiveness of the proposed model IEOPF on synthetic images that are widely used to verify ACMs and selected natural images from public datasets. We then evaluate the proposed model on two pubic MR brain image repositories qualitatively and quantitatively. Unless otherwise specified, we set $a = 2.0$, $\Delta t = 0.1$, $\lambda_1 = \lambda_2 = \lambda_3 = 1.0$, $\mu = 1.0$, and $\nu = 0.005 \times 255 \times 255$ in this paper.

4.1. Effectiveness of IEOPF

In this subsection, we qualitatively evaluate effectiveness of the proposed model on synthetic images and selected natural images from public datasets and give the validation results in the following paragraphs. Note that the synthetic and natural images are either widely used in the literature to verify active contour models or appropriate for application of the proposed model IEOPF.

We first applied the proposed model to three synthetic gray images (*widely used to evaluate active contour models in the literature*), one cardiac X-ray image, and one brain MR image in this subsection. It is obvious that segmentation results of the proposed model on the images are agreed with contents contained in the images even though intensities of the images are not homogeneous due to existing of severe intensity biases as shown in Fig. 3. That is to say that it is difficult to extract interested objects from the images because intensity ranges of objects (including the background) in the images are overlapped due to severe intensity inhomogeneities existed in the images which manifests as there are no well-separated peaks in intensity histograms of the images as shown in Fig. 3. However, there are well-defined and separated peaks in histograms of the bias corrected images, each corresponding to one object or the background. This demonstrates the capability of the proposed model in correcting bias fields from images with intensity inhomogeneity. Meanwhile, the biases estimated by the proposed model with orthogonal primary functions are all slowly (not sharply) varying as shown in Fig. 3 which meets properties of the bias field as described in section 1.

We then applied the proposed two phase level set model to segment four selected natural images with three color channels from BSD database [29], namely 135069, 42049, 3096, and 86016, respectively. *The reason we selected these images is that each of the images contains only one object besides the background which can therefore be distinguished with one level set function.* Results of the proposed model on segmentation of the images with two phase level sets are given in Fig. 4. It is obvious that the estimated biases are smoothly varying and the corrected images are more homogeneous than the originals. Furthermore, the energy functional of the proposed model defined in Eq.(17) is converged (generally in less than 50 iterations) as shown in the right column of Fig. 4.

We thirdly applied the proposed three phase level set model to segment two MR brain images which are corrupted by severe intensity inhomogeneities and two selected natural images from MSRCORID database [30], namely, 164.6484 and 112.1204. *The first two images are widely used to evaluate multiple phase active contour models in the literature and the last two images are selected because three kind of objects are*

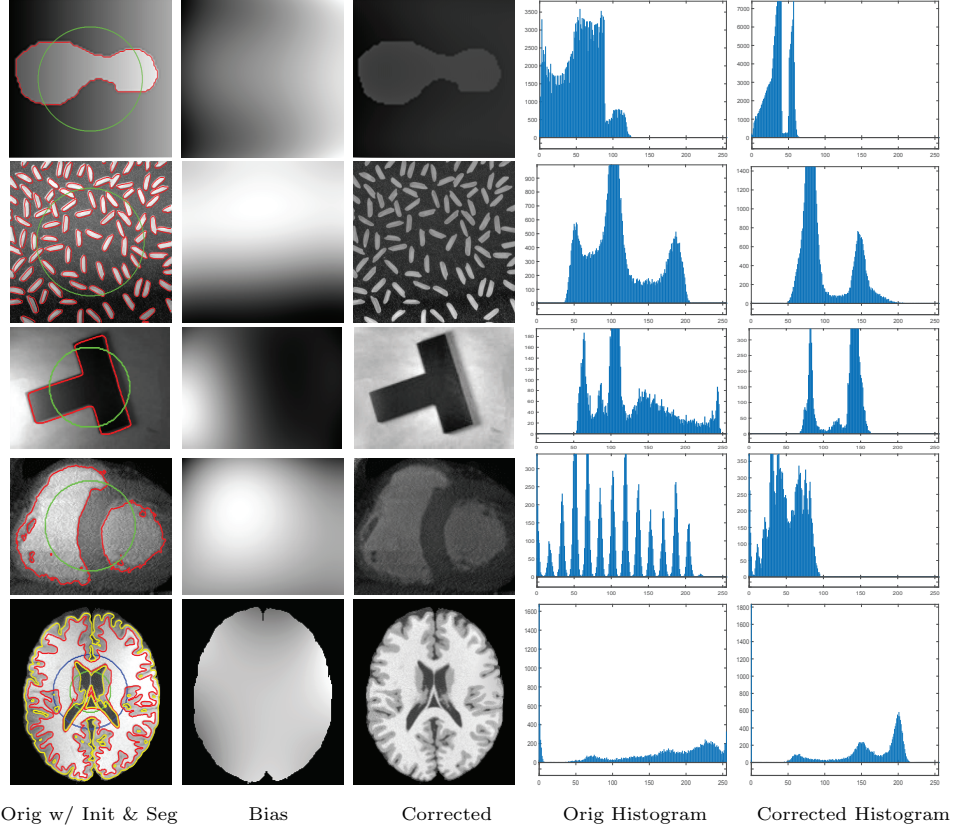


Figure 3: Results of IEOPF in segmenting inhomogeneous gray images and correcting the biases.

contained which are suitable for three phase segmentation. From the results given in Fig. 5, we can see that the estimated biases are smooth and the corrected images are much more homogeneous. Moreover, the extracted objects are coincided with the images.

We fourthly evaluate energy convergence of the proposed model on all above mentioned images and show iteration process of the proposed model on four of them in Fig. 6. *The images are appropriate to evaluate the proposed model in the sense of one-channel-two-phase, one-channel-multiple-phase, multiple-channel-two-phase, and multiple-channel-multiple-phase, respectively.* It can be seen that the proposed model is convergent and satisfactory results can be generally obtained in less than 20 iterations. Note that three kinds of color are used to show the results clearly.

We finally compare results of the proposed model with state-of-the-art models on one synthetic image and one natural image from BSD qualitatively and show the result in Fig. 7. *Note that to be fair, initializations on either image are all the same for each of the comparable models.* And we set the parameters $\lambda_1 = \lambda_2 = 1.0$, $\mu = 1.0$, and $\nu = 0.005 \times 255 \times 255$. As the CV, RSF, LIC, and LINC models are short of the capability to extract interested objects from color images directly, we first convert the color image to a gray image using the `rgb2gray` function of matlab and then input the image to the models. However, the proposed

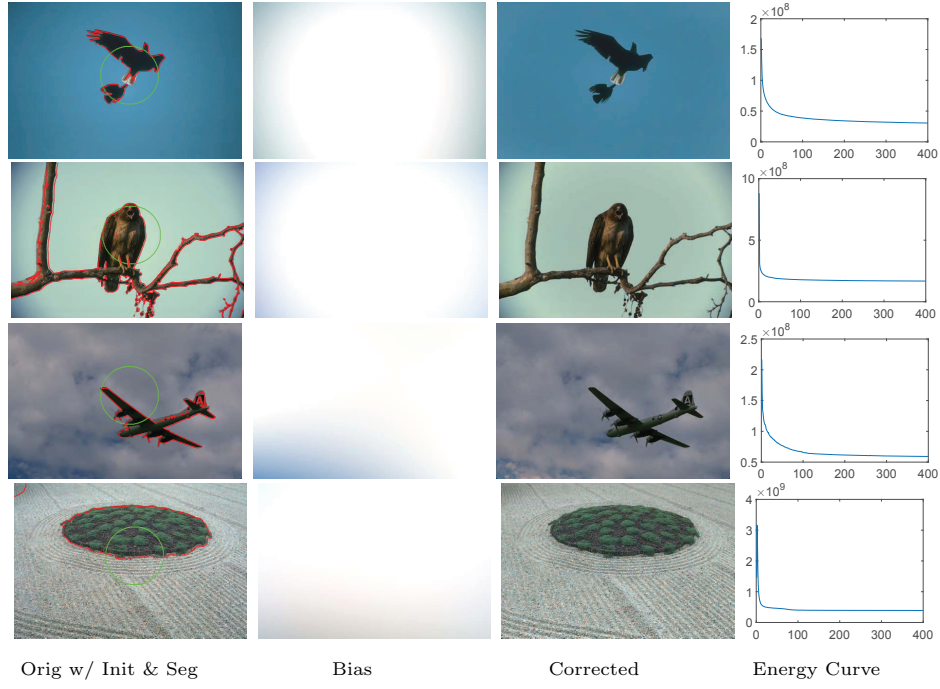


Figure 4: Results of IEOPF₃² in segmenting natural images from BSD database.

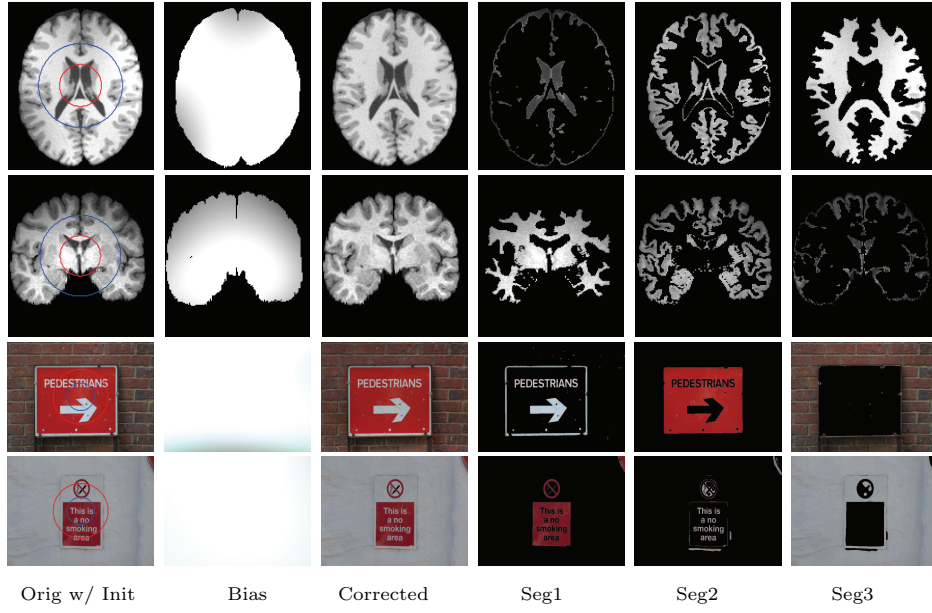


Figure 5: Results of IEOPF₁³ and IEOPF₃³ in segmenting brain MR images and natural images from MSRCORID database, respectively.

model can be directly used to deal with color images (three channels). Therefore, segmentation contour of the proposed model on the natural image given is marked on the original colourful image whereas results

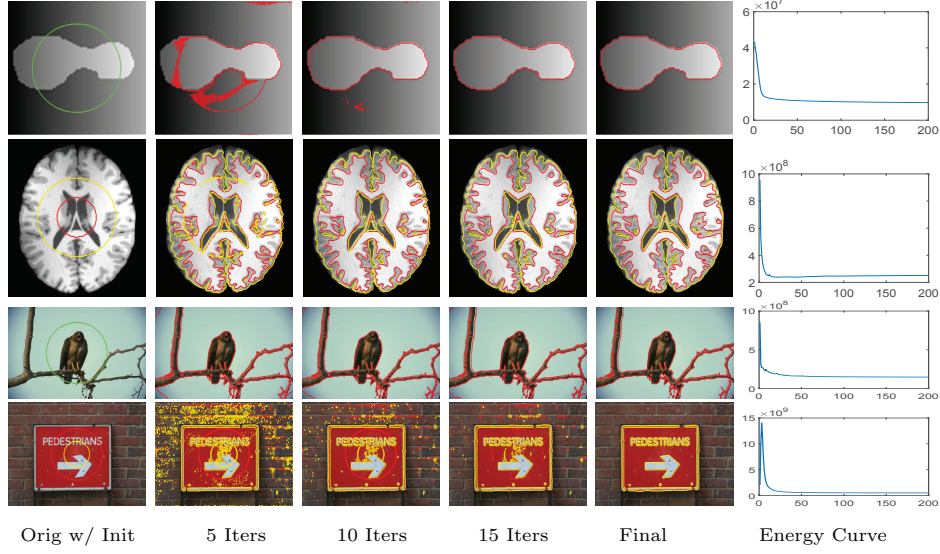


Figure 6: Demonstration of 0-level contour evolutions of the proposed model IEOPF.

of the others are marked on the gray images. As shown in Fig. 7, due to absence of dealing with intensity inhomogeneity, segmentation results of the CV model include other regions besides geometrical shapes really exist in the synthetic image and eagles in the natural image. Segmentation results of the RSF model are a little better than those of the CV model because it can handle intensity inhomogeneity to some extent. But the RSF model lacks the capability of bias estimation and correction. As shown in Fig. 7, the bias fields estimated by the LIC model are obviously not smooth enough and segmentation results are certainly wrong. Although segmentation results and bias estimations of the LINC model are desirable, color images can not be directly input into the model before being converted to gray ones. In addition, as mentioned in section 1, convolution operation in the evolution results in a heavy computational burden for LINC which we will further discuss in section 5.2. It obvious that the proposed model achieves the best segmentations, bias estimations and corrections.

4.2. Evaluation on pubic image repositories

In this subsection, we evaluate effectiveness of the proposed model quantitatively on one simulated MR dataset and one real MR image dataset. The first one consist of 9 cases of MR images with three different levels of noise and intensity inhomogeneity, respectively. Resolutions of the images are $181 \times 217 \times 181$ with 1 mm in-plane pixel size and 1 mm slice thickness. For more information about the dataset, interested readers are referred to the website <http://brainweb.bic.mni.mcgill.ca/brainweb/> and the reference [31]. To construct a much more challenging dataset for segmentation methods, three more levels of non-linear intensity inhomogeneities are added to the original image with noises. Therefore, there are totally 18 image cases for the first image dataset. The second image set is known worldwide as the Internet

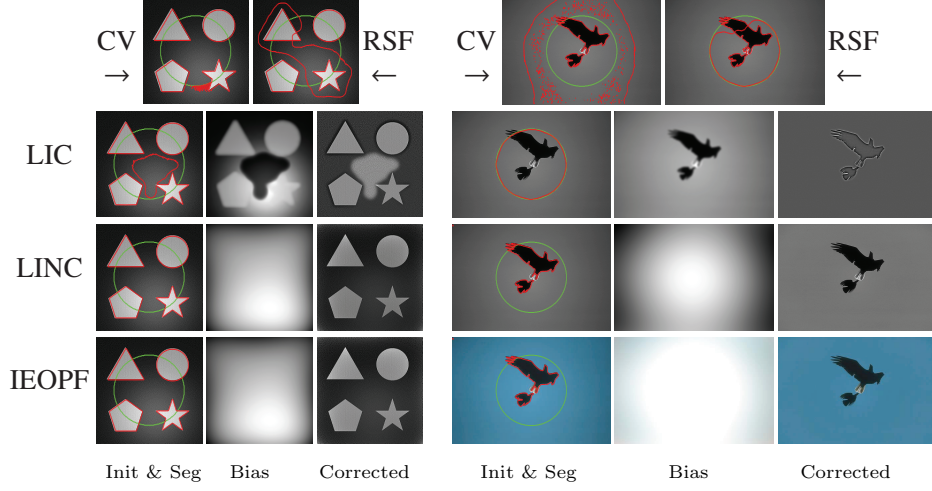


Figure 7: Qualitative comparison with state-of-the-art models on one synthetic image (left) and one natural image from BSD (right).

Brain Segmentation Repository (IBSR) which contains 18 cases of T1-weighted brain MR image cases with skull-removed masks and manually-guided expert segmentation results. Resolutions of the images are all $256 \times 128 \times 256$. Interested readers are referred to <https://www.nitrc.org/projects/ibsr> for detail. Note that for each image case, the segmentation task is to extract white matter (WM), gray matter (GM), and cerebrospinal fluid (CSF) from the background. As intensities of the background are all zero for the images, two level set functions are used to partition the images into three regions that is $K = 2$ and $N = 3$. To compare performance of the proposed model with state-of-the-art models like CV, LIC, and LINC on these image datasets, we first extend the comparable models to three phase (matlab codes will be released on our personal homepage if this paper got published). We then define membership functions $M_1 = (1 - H(\phi_1))(1 - H(\phi_2))$, $M_2 = (1 - H(\phi_1))H(\phi_2)$, and $M_3 = H(\phi_1)$ to represent WM, GM, and CSF, respectively. For a fair comparison, we first extend comparison models to three phase and then use the same parameter set and the same strategy to initialize the level set functions for all the comparison models. The initialization strategy is that areas separated by a predefined threshold are adopted to initialize ϕ_1 by considering the areas as inside and outside of the zero level contour. Areas separated by another predefined threshold are adopted to initialize the level set function ϕ_2 . The thresholds are adaptively defined as 0.8 and 0.3 times of maximal intensity of pending to be segmented images. We have to point out that the proposed model is robust to initialization which will be discussed in section 5.3. Note that we applied the proposed model and comparable state-of-the-art models only on image slices that really contain WM, GM, and CSF.

4.2.1. Qualitative comparison

Segmentation results of the proposed model and three state-of-the-art methods on the 90-th slice of selected brainweb cases and the 128-th slice of selected IBSR image cases are given in Fig. 8 and Fig. 10.

The corresponding bias estimation and correction results are given in Fig. 9 and Fig. 11, respectively. The reason we select these image is that they are the most noisy and biased and they are therefore challengeable. It can be seen that 1) the proposed model is much more robust to noises and bias fields and 2) segmentation results of the proposed model are much more close to corresponding ground truth. Quantitative evaluation will be given in section 4.2.2.

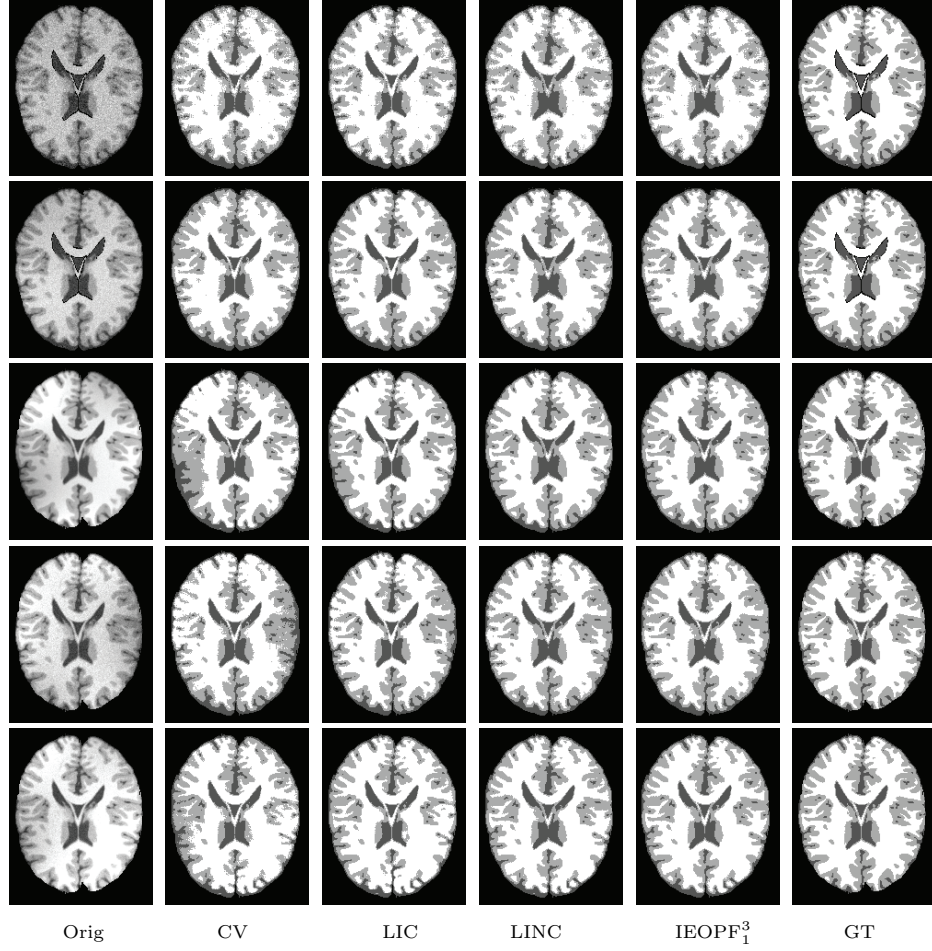


Figure 8: Segmentation comparison with state-of-the-art models on selected BrainWeb images.

4.2.2. Quantitative evaluation

To quantitatively evaluate segmentation results of the proposed framework with state-of-the-art method, false positive ratio (FPR), false negative ratio (FNR), and dice similarity coefficient (DSC) are metrics used in this paper. Let NFP and NFN be the number of FP (false positive) and FN (false negative) and A be the ground truth, FPR and FNR can then be defined by

$$FPR = \frac{NFP}{|I| - |A|} \quad (27)$$

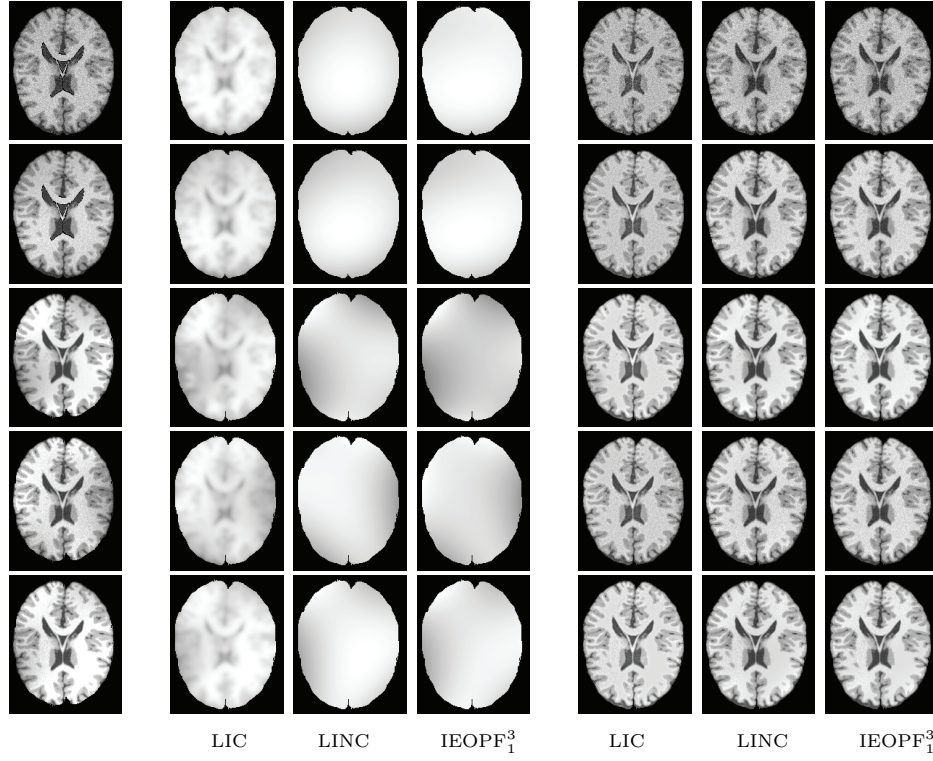


Figure 9: Comparison of bias estimation and correction with state-of-the-art methods on selected BrainWeb images.

and

$$FNR = \frac{NFN}{|A|} \quad (28)$$

respectively. Pairwise vertical mouldings denote size of the contained region. As well known, values of FPR and FNR are both in $[0, 1]$ with a smaller value indicating a better match between the segmentation and the ground truth. On the other side, the definition DSC can be written as

$$DSC = \frac{2|A \cap B|}{|A| + |B|} \quad (29)$$

where \cap is the intersection operator. Values of DSC are in the interval of $[0, 1]$ with a higher value indicating a better match between the segmentation result B and the ground truth A.

Quantitative comparison of segmentation results of the proposed model with state-of-the-art models on the BrainWeb and IBSR images in terms of FPR, FNR, and DSC are given in Fig. 12 and Fig. 13, respectively. For the BrainWeb dataset, it can be seen that boxes of WM, GM, and CSF of the proposed model in terms of FPR and FNR are much more compacted and the mediums are lower than CV, LIC, and LINC which indicates segmentation results of the proposed model match better with corresponding ground truth than state-of-the-art models. On the contrary, boxes of WM, GM, and CSF of the proposed model in terms of DSC are also compacted but the mediums are higher than CV, LIC, and LINC which

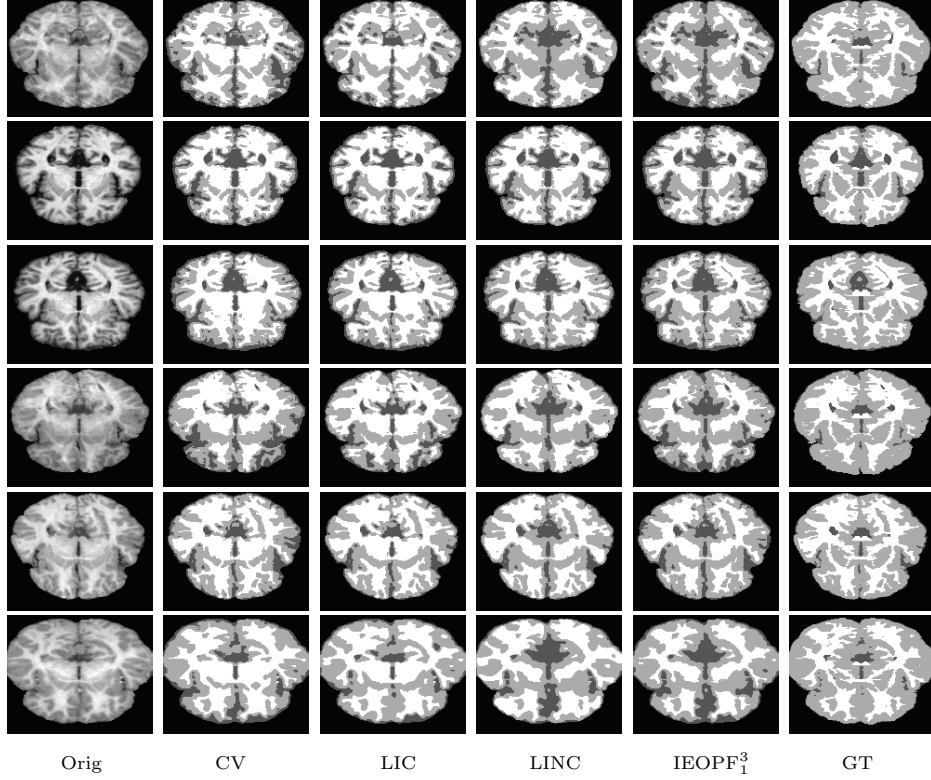


Figure 10: Segmentation comparison with state-of-the-art methods on selected IBSR images.

indicates better match of the segmentation results with corresponding ground truth. On the other side, for the IBSR dataset, FPR boxes of WM and FNR boxes of GM and CSF are more compacted and lower than state-of-the-art models. DSC boxes of WM, GM, and CSF are more compacted than other models with medium values similar to CV but higher than LIC and LINC. As shown in Fig. 10, biases of IBSR images are weak than BrainWeb and ground truths in IBSR images consider more non-zero area as gray matter and therefore decrease areas of WM and CSF. This is the main reason that performance of the proposed model on IBSR is worse than that on BrainWeb images.

5. Discussions

5.1. Relationship with CV and PS

It is worth pointing out that the proposed energy \mathcal{F} in Eq. (14) reduces to the first term of Eq. (2) when 1) $\lambda_1 = \lambda_2 = 1.0$, and 2) $w_1 = 1.0$ and $w_i = 0$ for $i = 2, 3, \dots, M$ which indicates $b(\mathbf{x}) = \mathbf{1}$. That is to say the proposed model $IEOPF^2$ defined in Eq. (14) is a generalization of the well known Chan-Vese model. If we define $u_i(\mathbf{x}) = \mathbf{w}^T G(\mathbf{x}) c_i$, the energy defined in Eq. (14) will reduce to the first term of Eq. (3) and the smoothness of $u_i(\mathbf{x})$ are ensured by the orthogonal primary functions g_1, g_2, \dots , and g_M implied in G . Therefore, no further regularization term like the second term in Eq. (3) are needed to smooth $u_i(\mathbf{x})$.

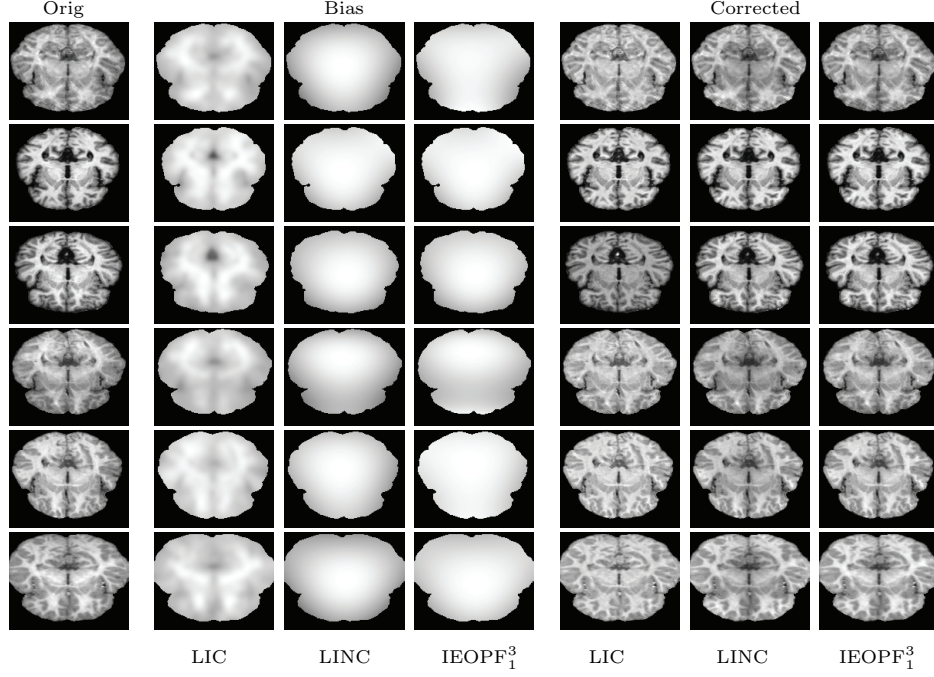


Figure 11: Comparison of bias estimation and correction with state-of-the-art methods on selected IBSR images.

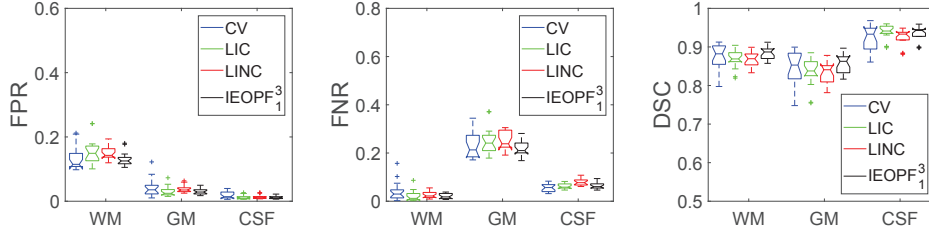


Figure 12: Quantitative comparison with state-of-the-art methods on BrainWeb images.

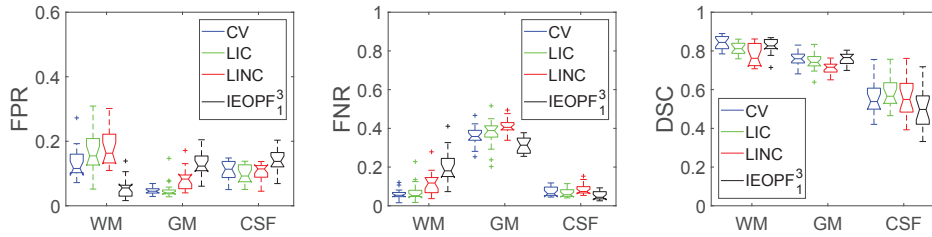


Figure 13: Quantitative comparison with state-of-the-art methods on IBSR images.

5.2. Improvement to LINC

As described in [27], in the case of two phase implementation of the LINC model, there are 7 convolutions in the size of normalized kernel K for each iteration of the level set function, which are the main factor causing computational burden of LINC. As smoothness of bias fields existing in images with inhomogeneous

intensities can be guaranteed by orthogonal primary functions, the proposed model IEOPF removes the convolution kernel K from the LINC model and therefore there is no convolution in iterations of the level set function any more.

5.3. Robustness of IEOPF to Initialization

As mentioned above, the proposed model is a generalization of CV and a simplification of LINC. It is well known that the intensity constants in CV can be seen as global average of inside and outside regions separated by the 0-level set contour. Therefore, CV is greatly non-sensitive to local intensities and robust to initialization [16]. On the other side, as pointed out in [27], LINC is also robust to initialization. Thus, as a generalization of CV and a simplification of LINC, the proposed model is robust to initialization. We give a demonstration of the proposed model on one vessel image in four initialization strategies in Fig. 14 to verify robustness of the proposed model to initialization. It is obvious that there are not obvious differences between any two strategies in terms of bias estimation and final segmentations, which proves that the proposed model is robust to initialization.

5.4. Impact of weighting coefficients

For three phase segmentation of the proposed model on BrainWeb and IBSR datasets where $M_1 = (1 - H(\phi_1))(1 - H(\phi_2))$, $M_2 = (1 - H(\phi_1))H(\phi_2)$, and $M_3 = H(\phi_1)$, the formulation in Eq. (20) can be rewritten into

$$\begin{aligned} \frac{\partial \phi_1}{\partial t} &= -\delta(\phi_1)(-\lambda_1 e_1(1 - H(\phi_2)) - \lambda_2 e_2 H(\phi_2) + \lambda_3 e_3) \\ &+ \mu \left(\nabla^2 \phi_1 - \operatorname{div} \left(\frac{\nabla \phi_1}{|\nabla \phi_1|} \right) \right) + \nu \delta(\phi_1) \operatorname{div} \left(\frac{\nabla \phi_1}{|\nabla \phi_1|} \right) \end{aligned} \quad (30)$$

and

$$\begin{aligned} \frac{\partial \phi_2}{\partial t} &= -\delta(\phi_2)(-\lambda_1 e_1(1 - H(\phi_1)) + \lambda_2 e_2(1 - H(\phi_1))) \\ &+ \mu \left(\nabla^2 \phi_2 - \operatorname{div} \left(\frac{\nabla \phi_2}{|\nabla \phi_2|} \right) \right) + \nu \delta(\phi_2) \operatorname{div} \left(\frac{\nabla \phi_2}{|\nabla \phi_2|} \right). \end{aligned} \quad (31)$$

It is obvious that $e_i(\mathbf{x}) \geq 0$ in Eq. (20) and $M_i \in [0, 1]$ where $i = 1, 2, 3$. Therefore, the first term on the right hand of Eq. (30) is monotone increasing for λ_1 and λ_2 and decreasing for λ_3 respectively, only if they take positive values. Thus, given a positive increment on λ_1 and λ_2 , the level set function ϕ_1 will be increased much harder in each iteration. On the contrary, given a positive increment on λ_3 , ϕ_1 will be decreased much harder. As described in Algorithm 1, we let the level set functions take negative and positive values inside and outside the 0-level set contours, respectively. Hence, for all the others fixed, the greater the coefficient λ_1 and λ_2 are, the smaller the region inside the 0-level set contour is, and vice versa. Similarly, the greater the coefficient λ_3 is, the smaller the region outside the 0-level set contour is, and vice versa. Same analysis

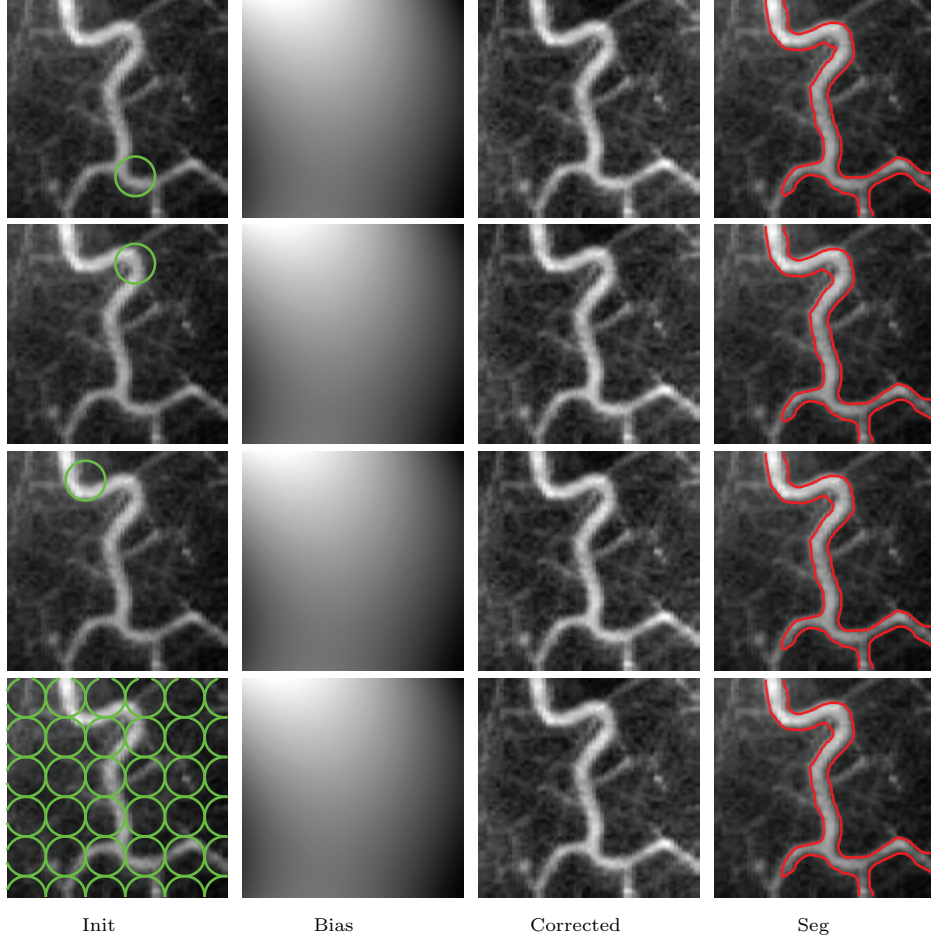


Figure 14: Demonstration of robustness to initialization of the proposed model.

can be applied to Eq. (31) to conclude that the greater the coefficient λ_1 and λ_2 are, the smaller the regions inside and outside the 0-level set contour are, and vice versa. As mentioned earlier, the regularization term and arc length term are used to maintain regularity of the level set function and smooth 0-level set contour. Thus, the greater the parameters μ and ν are, the level set function is more close to sign distance function and the smoother the 0-level set contour is.

6. Conclusion and future work

The proposed model is effective in segmenting images with inhomogeneous intensities and provide a smooth bias estimation of the inhomogeneity. We will further improve the proposed model to extract brain tissues in 3D on public image repositories in our future work.

Acknowledgments

This work was supported by the National Natural Science Foundation of China and the Fundamental Research Funds for the Central Universities of China under grant Nos. 61602101 and N140403006, respectively.

References

- [1] C. Feng, D. Zhao, M. Huang, Image segmentation using CUDA accelerated non-local means denoising and bias correction embedded fuzzy c-means (BCEFCM), *Signal Processing* 122 (2016) 164–189.
- [2] N. Paragios, R. Deriche, Geodesic active regions and level set methods for supervised texture segmentation, *International Journal of Computer Vision* 46 (3) (2002) 223–247.
- [3] C. Feng, D. Zhao, M. Huang, Segmentation of ischemic stroke lesions in multi-spectral MR images using weighting suppressed FCM and three phase level set, in: *International Workshop on Brainlesion: Glioma, Multiple Sclerosis, Stroke and Traumatic Brain Injuries*, Springer, 2015, pp. 233–245.
- [4] C. Feng, D. Zhao, M. Huang, Segmentation of longitudinal brain MR images using bias correction embedded fuzzy c-means with non-locally spatio-temporal regularization, *Journal of Visual Communication and Image Representation* 38 (2016) 517–529.
- [5] N. Paragios, R. Deriche, Geodesic active contours and level sets for the detection and tracking of moving objects, *IEEE Transactions on pattern analysis and machine intelligence* 22 (3) (2000) 266–280.
- [6] L. He, Z. Peng, B. Everding, X. Wang, C. Y. Han, K. L. Weiss, W. G. Wee, A comparative study of deformable contour methods on medical image segmentation, *Image and Vision Computing* 26 (2) (2008) 141–163.
- [7] M. Kass, A. Witkin, D. Terzopoulos, Snakes: Active contour models, *International journal of computer vision* 1 (4) (1988) 321–331.
- [8] S. Menet, P. Saint-Marc, G. Medioni, Active contour models: Overview, implementation and applications, in: *Systems, Man and Cybernetics, 1990. Conference Proceedings.*, IEEE International Conference on, IEEE, 1990, pp. 194–199.
- [9] S. Osher, R. P. Fedkiw, Level set methods: an overview and some recent results, *Journal of Computational physics* 169 (2) (2001) 463–502.
- [10] S. Osher, N. Paragios, *Geometric level set methods in imaging, vision, and graphics*, Springer Science & Business Media, 2003.
- [11] N. Paragios, A level set approach for shape-driven segmentation and tracking of the left ventricle, *IEEE transactions on medical imaging* 22 (6) (2003) 773–776.
- [12] C. Feng, S. Zhang, D. Zhao, C. Li, Simultaneous extraction of endocardial and epicardial contours of the left ventricle by distance regularized level sets, *Medical Physics* 43 (6) (2016) 2741–2755.
- [13] C. Li, C. Xu, C. Gui, M. D. Fox, Distance regularized level set evolution and its application to image segmentation, *IEEE Transactions on Image Processing* 19 (12) (2010) 3243–3254.
- [14] K. Zhang, H. Song, L. Zhang, Active contours driven by local image fitting energy, *Pattern recognition* 43 (4) (2010) 1199–1206.
- [15] D. Mumford, J. Shah, Optimal approximations by piecewise smooth functions and associated variational problems, *Communications on pure and applied mathematics* 42 (5) (1989) 577–685.
- [16] T. F. Chan, L. A. Vese, Active contours without edges, *IEEE transactions on Image processing* 10 (2) (2001) 266–277.
- [17] L. A. Vese, T. F. Chan, A multiphase level set framework for image segmentation using the Mumford and Shah model, *International journal of computer vision* 50 (3) (2002) 271–293.

- [18] X.-F. Wang, D.-S. Huang, H. Xu, An efficient local Chan–Vese model for image segmentation, *Pattern Recognition* 43 (3) (2010) 603–618.
- [19] S. Liu, Y. Peng, A local region-based Chan–Vese model for image segmentation, *Pattern Recognition* 45 (7) (2012) 2769–2779.
- [20] A. Tsai, A. Yezzi Jr, A. S. Willsky, Curve evolution implementation of the Mumford-Shah functional for image segmentation, denoising, interpolation, and magnification, *IEEE Transactions on Image Processing* 10 (8) (2001) 1169–1186.
- [21] L. Wang, L. He, A. Mishra, C. Li, Active contours driven by local Gaussian distribution fitting energy, *Signal Processing* 89 (12) (2009) 2435–2447.
- [22] C. Li, C.-Y. Kao, J. C. Gore, Z. Ding, Minimization of region-scalable fitting energy for image segmentation, *IEEE Transactions on Image Processing* 17 (10) (2008) 1940–1949.
- [23] K. Ni, X. Bresson, T. Chan, S. Esedoglu, Local histogram based segmentation using the Wasserstein distance, *International journal of computer vision* 84 (1) (2009) 97–111.
- [24] Q. Ge, L. Xiao, J. Zhang, Z. H. Wei, An improved region-based model with local statistical features for image segmentation, *Pattern Recognition* 45 (4) (2012) 1578–1590.
- [25] X.-F. Wang, H. Min, L. Zou, Y.-G. Zhang, A novel level set method for image segmentation by incorporating local statistical analysis and global similarity measurement, *Pattern Recognition* 48 (1) (2015) 189–204.
- [26] C. Li, R. Huang, Z. Ding, J. C. Gatenby, D. N. Metaxas, J. C. Gore, A level set method for image segmentation in the presence of intensity inhomogeneities with application to MRI, *IEEE Transactions on Image Processing* 20 (7) (2011) 2007–2016.
- [27] C. Feng, D. Zhao, M. Huang, Image segmentation and bias correction using local inhomogeneous iNtensity clustering (LINC): A region-based level set method, *Neurocomputing* 219 (2017) 107–129.
- [28] M. Powell, *Approximation theory and methods*, Cambridge: Cambridge University Press, 1981.
- [29] P. Arbelaez, M. Maire, C. Fowlkes, J. Malik, Contour detection and hierarchical image segmentation, *IEEE Trans. Pattern Anal. Mach. Intell.* 33 (5) (2011) 898–916.
- [30] Microsoft, Microsoft research cambridge object recognition image database, <http://research.microsoft.com/en-us/downloads/b94de342-60dc-45d0-830b-9f6eff91b301/default.aspx> (2005).
- [31] C. A. Cocosco, V. Kollokian, R. K.-S. Kwan, G. B. Pike, A. C. Evans, Brainweb: Online interface to a 3D MRI simulated brain database, in: *NeuroImage*, Citeseer, 1997.